Supporting Information

Greenery-Inspired Nanoengineering of Bamboo-Like Hierarchical Porous Nanotubes with Spatially Organized Bifunctionalities for Synergistic Photothermal Catalytic CO$_2$ Fixation

Yingchun Guo,[a] Weijia Chen,[b] Lei Feng,[b] Yanchen Fan,[c] Jinsheng Liang,*[a] Xiaomei Wang*[b] and Xu Zhang*[b]

[a] Key Laboratory of Special Functional Materials for Ecological Environment and Information, School of Materials Science and Engineering, Hebei University of Technology, Ministry of Education, Tianjin 300130, China

[b] Hebei Key Laboratory of Functional Polymers, School of Chemical Engineering and Technology, Hebei University of Technology, Tianjin 300130, China

[c] School of Materials Science and Engineering, Beihang University, Beijing 100191, China

*Corresponding Author: E-mail: xmwang@hebut.edu.cn; xuzhang@hebut.edu.cn; liangjinsheng@hebut.edu.cn

Experimental Section

Chemicals. All chemicals were purchased from commercial supplies and used without further purification. Nickel nitrate hexahydrate ($Ni(NO_3)_2 \cdot 6H_2O$, 98%), Zinc nitrate hexahydrate ($Zn(NO_3)_2 \cdot 6H_2O$, 98%), 2-methylimidazole (2-MeIM, 99%), 2, 2′-azobis (isobutyronitrile) (AIBN, 99%), and 4-vinylbenzyl chloride (VBC) (99%) were received from Tianjin Fuchen Chemical Corporation. 1-vinyl-3-ethylimidazolium bromide (VEIMBr), anhydrous ferric (III) chloride ($FeCl_3$), 1, 2-dichloroethane (DCE), divinylbenzene (DVB, containing 80% divinylbenzene isomers), methanol (CH_3OH, 99%), and concentrated sulfuric acid (H_2SO_4, 98 wt%) were obtained from Tianjin Hengshan Chemical Corporation. 3-bromopropylene oxide (99%), 2-butyloxirane (99%), 2-(phenoxymethyl)oxirane (99%), 2-phenyloxirane (99%), 2-((allyloxy)methyl)oxirane (99%), *p*-aminostyrene ($St-NH_2$, 96%) were received from Aladdin. Carbon dioxide and Ar gas were obtained from Tianjin Dongrun Gas Co., Ltd.

Characterizations. The morphology and structure were acquired by field-emission scanning electron microscopy with different accelerating voltage (SEM, FEI Nova NanoSEM450) and transmission electron microscopy (TEM, FEI Talos F200S, 200 kV). The aberration-corrected high-angle annular dark-field scanning transmission electron microscopy (AC-HAADF-STEM) measurements were taken on a Titan Themis Cubed G2 60-300, FEI. X-ray diffraction (XRD) patterns were investigated by a Bruker D8-Davinci equipped with Cu Kα radiation source. X-ray photoelectron spectroscopy (XPS) measurements were conducted on a Thermo Scientific ESCALab-250Xi spectrometer with monochromatic Al Kα radiation, and the binding energies were calibrated using the C 1s peak at 284.6 eV. Nitrogen adsorption-desorption isotherms were acquired on a surface area and porosity analyzer (Micromeritics ASAP 2020). The content of Ni atoms was investigated by an Optima 7300 DV inductively coupled plasma atomic emission spectrometer (ICP-AES). Fourier transform infrared (FT-IR) spectra were performed on a Bruker VECTOR-22 spectrometer. The ^{1}H-nuclear magnetic resonance (NMR)

spectra were analyzed and identified by a Bruker 400 spectrometer using $CDCl_3$ as a solvent and tetramethylsilane (TMS) as an internal standard. Electron paramagnetic resonance (EPR) spectra were collected by a Bruker EMXnano. Raman spectra were recorded on a Renishaw inVia Reflex UV Raman spectrometer with an excitation laser wavelength of $\lambda = 532$ nm. The obtained liquid solution after reaction was identified by GC–MS, and was quantitatively analyzed by GC equipped with flame ionization detector. Magnetic hysteresis loops of the materials were meansured at room temperature via vibrating sample magnetometer (VSM, MPMS XL-7).

Theoretical calculation details. All calculations in this work were performed using Gaussian 09 program package. Full geometry optimizations and the energies corrected by zero-point vibrational effects were performed to locate all the stationary points, using DFT/B3LYP/6-311G. The intrinsic reaction coordinate path was traced to check the energy profiles connecting each transition state to two associated minima of the proposed mechanism.
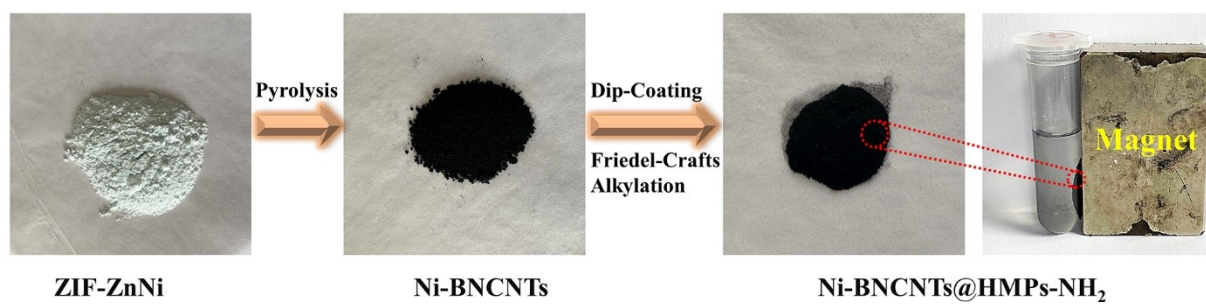
Figure S1. Photographs of the detailed fabrication process for the preparation of Ni-BNCNTs@HMPs-NH$_2$.
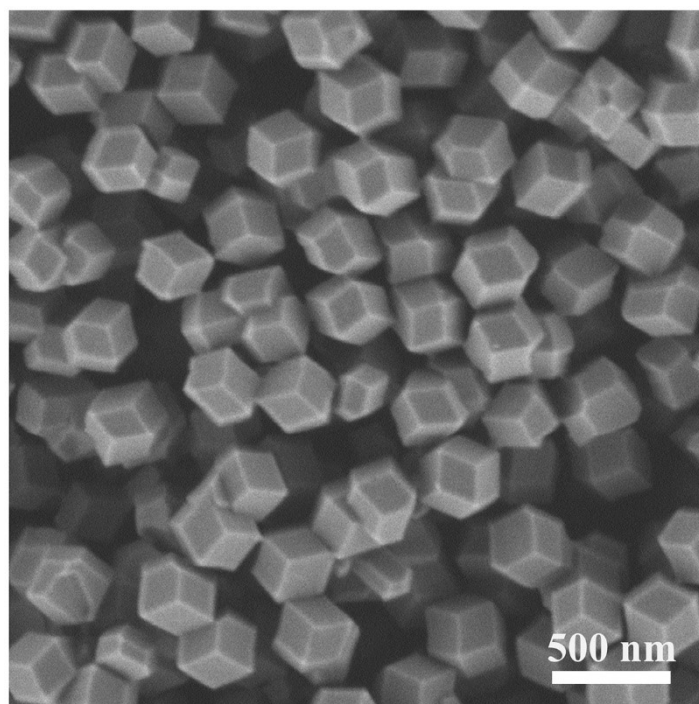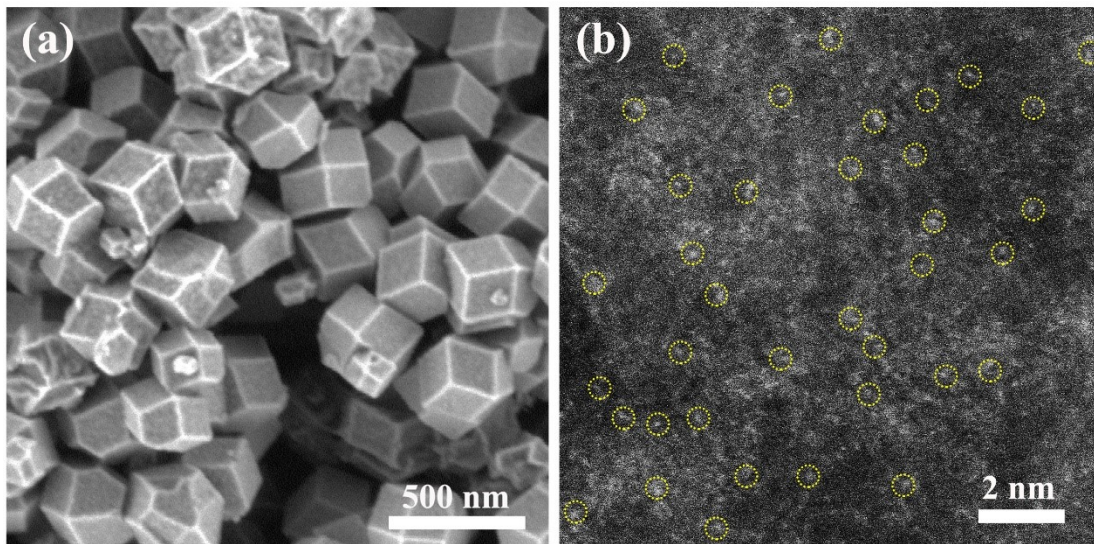
Figure S2. SEM image of the ZIF-ZnNi.

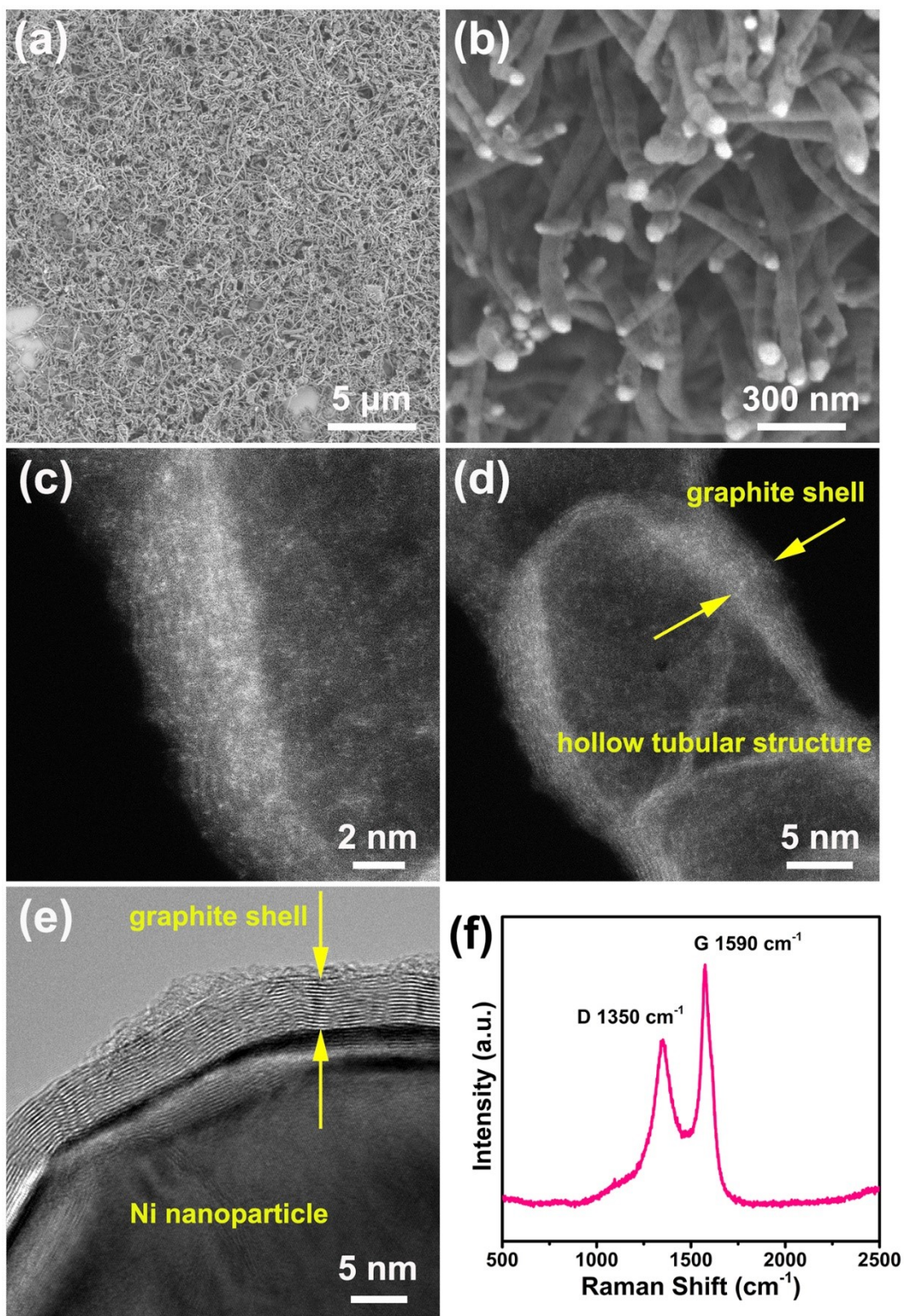**Figure S3.** (a) SEM image and (b) aberration-corrected HAADF-STEM image of the Ni-RDNC.

Figure S4. (a, b) SEM images, (c, d) aberration-corrected HAADF-STEM images, (e) TEM image, and (f) Raman spectrum of the Ni-BNCNTs.
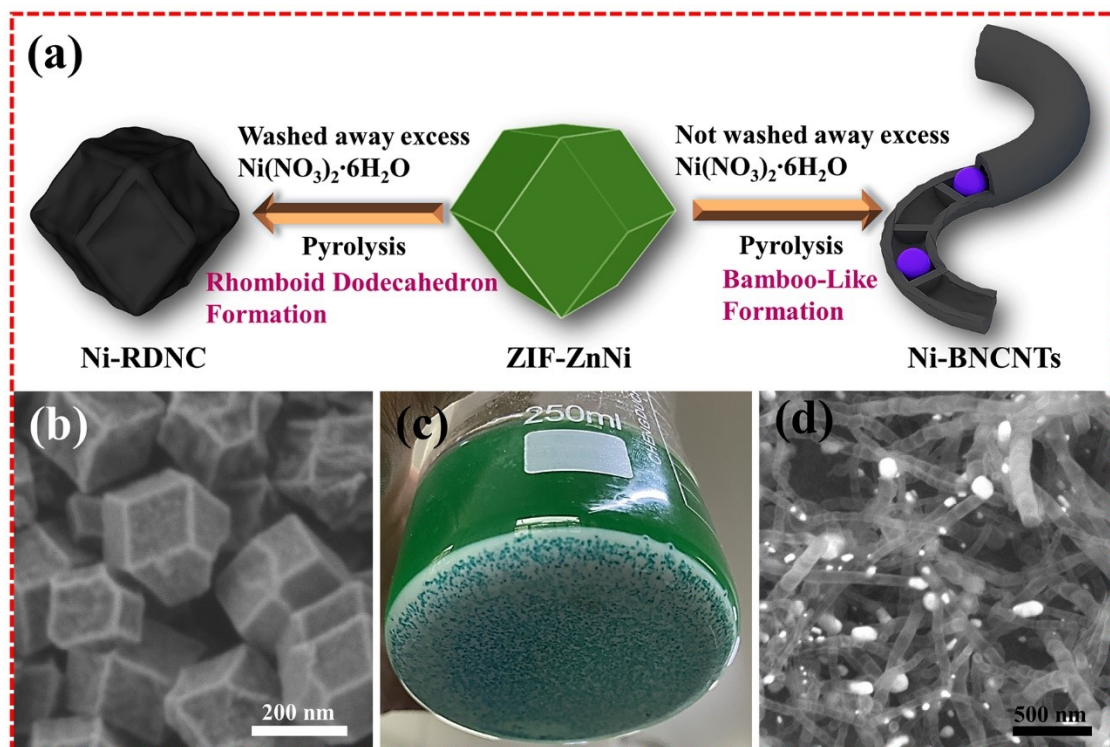
Figure S5. (a) Schematic illustration for the synthesis of Ni-RDNC and Ni-BNCNTs, (b) SEM image of Ni-RDNC, (c) Photograph of ZIF-ZnNi methanol solution, (d) SEM image of Ni-BNCNTs.

As shown in **Figure S5**, when the ratio of $Zn(NO_3)_2 \cdot 6H_2O$ and $Ni(NO_3)_2 \cdot 6H_2O$ is 1, there is a large amount of excess $Ni(NO_3)_2 \cdot 6H_2O$ (green granular) at the bottom of the beaker at the end of the reaction in addition to the production of ZIF-ZnNi (white powder). When the $Ni(NO_3)_2 \cdot 6H_2O$ was washed away, the rhombic dodecahedral structure remained after pyrolysis (**Figure S5b**), while when the $Ni(NO_3)_2 \cdot 6H_2O$ was not washed away, the bamboo-like nanotube structure was formed after pyrolysis (**Figure S5d**).
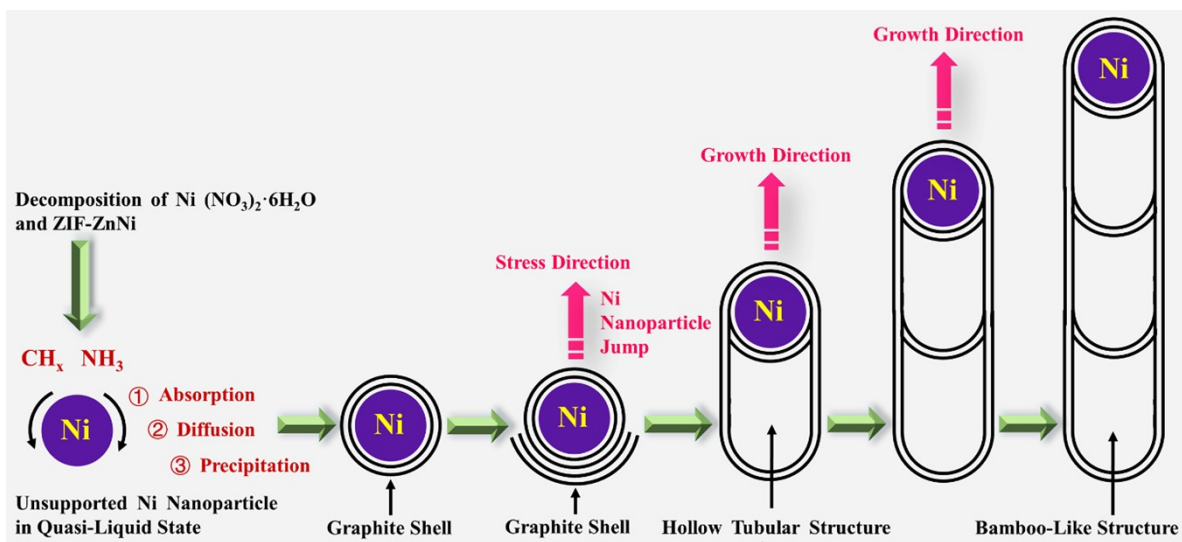
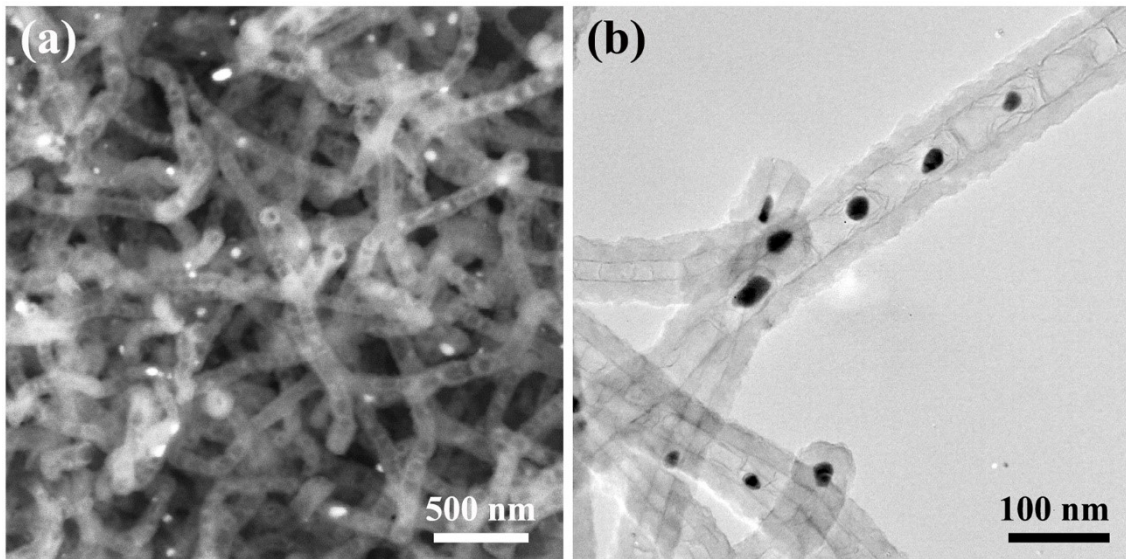**Figure S6.** Formation mechanism of bamboo-like carbon nanotubes.

Figure S7. (a) SEM image (concentric backscattered retractable detector at 5 kV) and (b) TEM image of the Ni-BNCNTs@HMPs-NH$_2$.
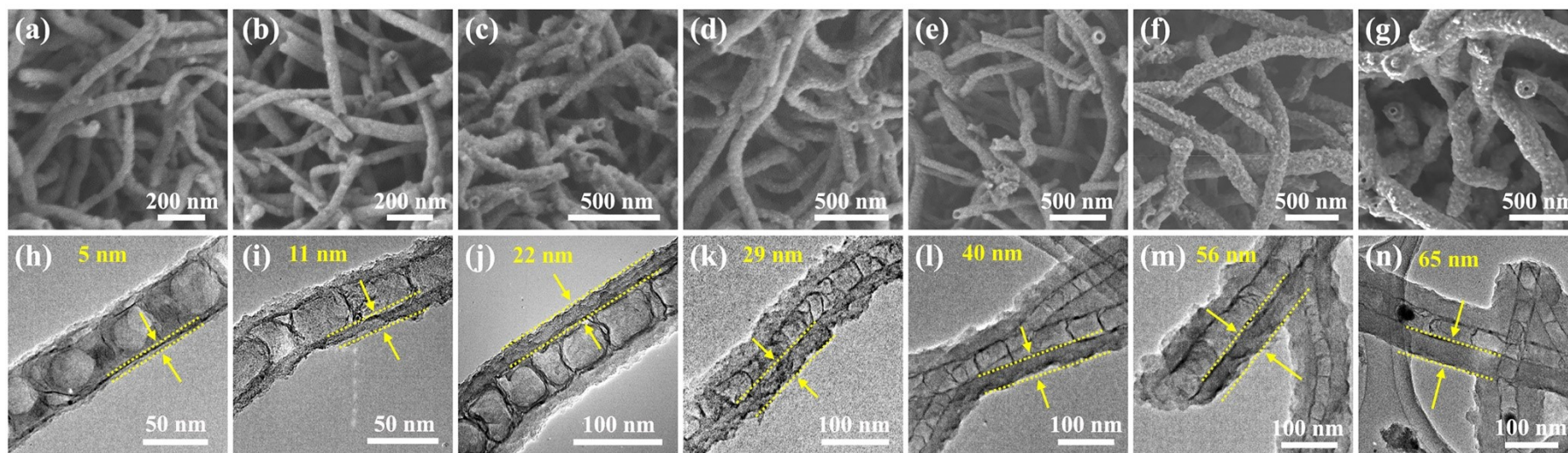
Figure S8. (a-g) SEM images and (h-n) TEM images of the Ni-BNCNTs@HMPs-NH$_2$ with different shell thickness prepared by different concentrations of precursors. The ratio of ethanol to mixed monomer is (a, h) 1.8 mL/5.0 mmol, (b, i) 1.6 mL/5.0 mmol, (c, j) 1.4 mL/5.0 mmol, (d, k) 1.2 mL/5.0 mmol, (e, l) 1.0 mL/5.0 mmol, (f, m) 0.8 mL/5.0 mmol, and (g, n) 0.6 mL/5.0 mmol.
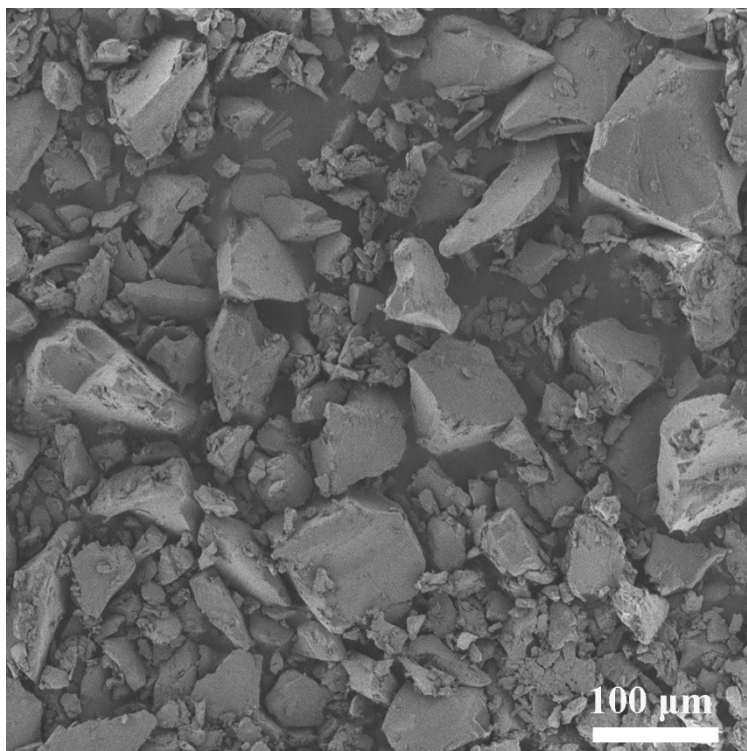
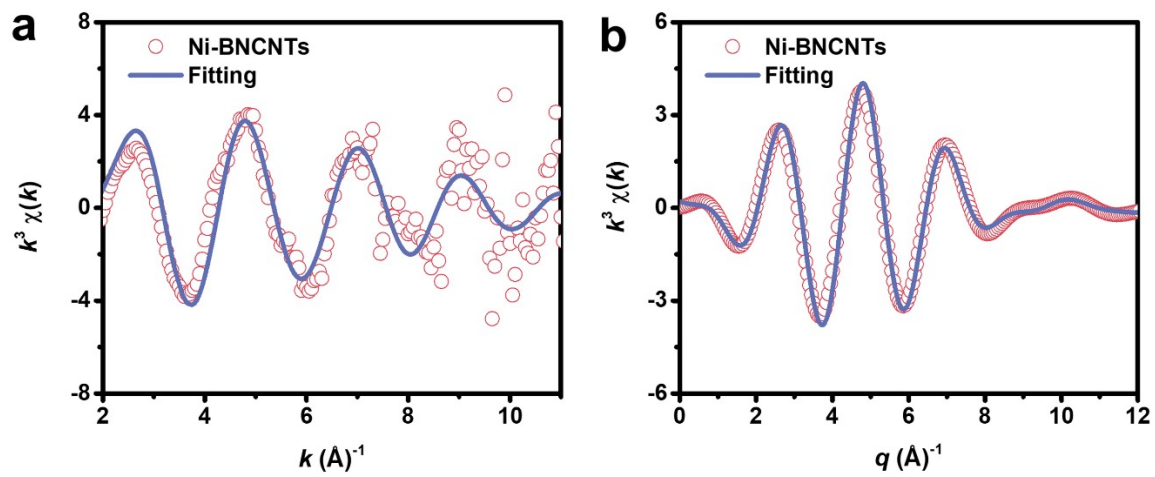**Figure S9.** SEM image of the HMPs-NH$_2$.

Figure S10. The corresponding FT-EXAFS (a) k-space and (b) q-space fitting curves of Ni-BNCNTs.
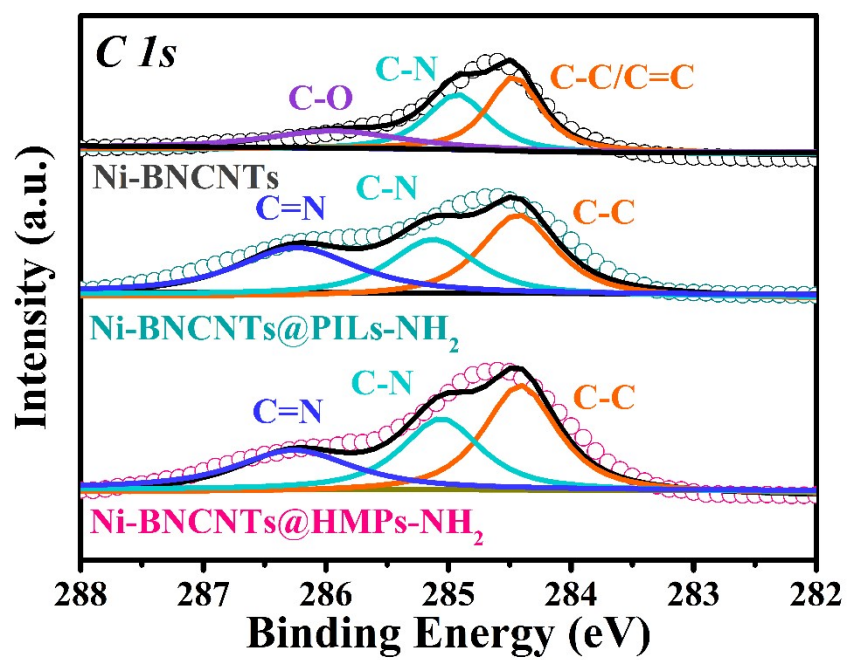
Figure S11. High-resolution XPS C 1s spectra of Ni-BNCNTs, Ni-BNCNTs@PILs-NH$_2$, and Ni-BNCNTs@HMPs-NH$_2$.
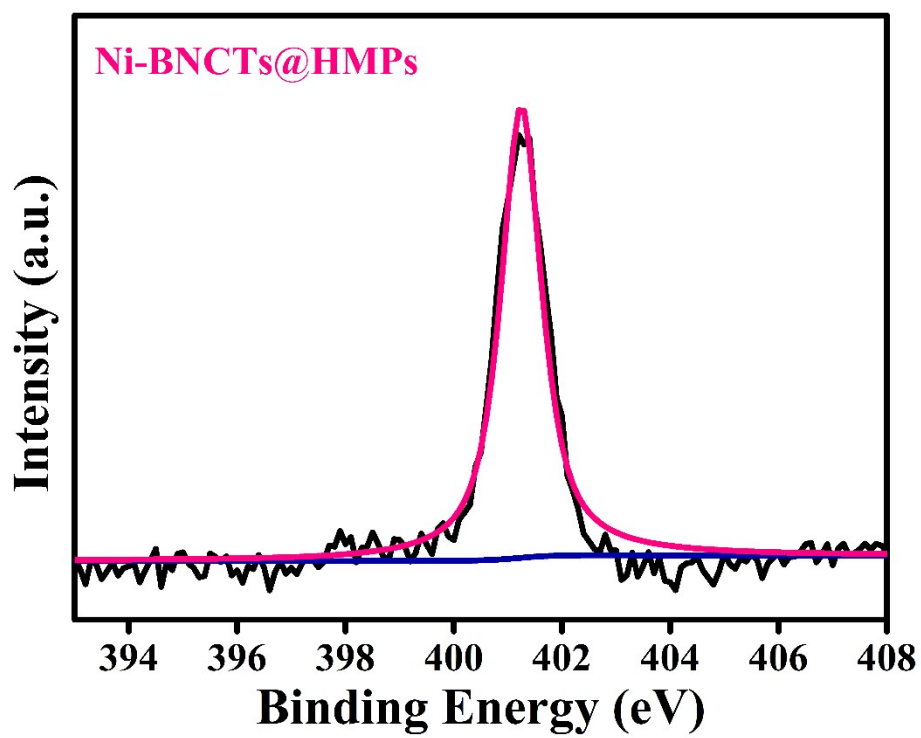
Figure S12. The XPS spectrum of high-resolution N 1s for Ni-BNCNTs@HMPs.
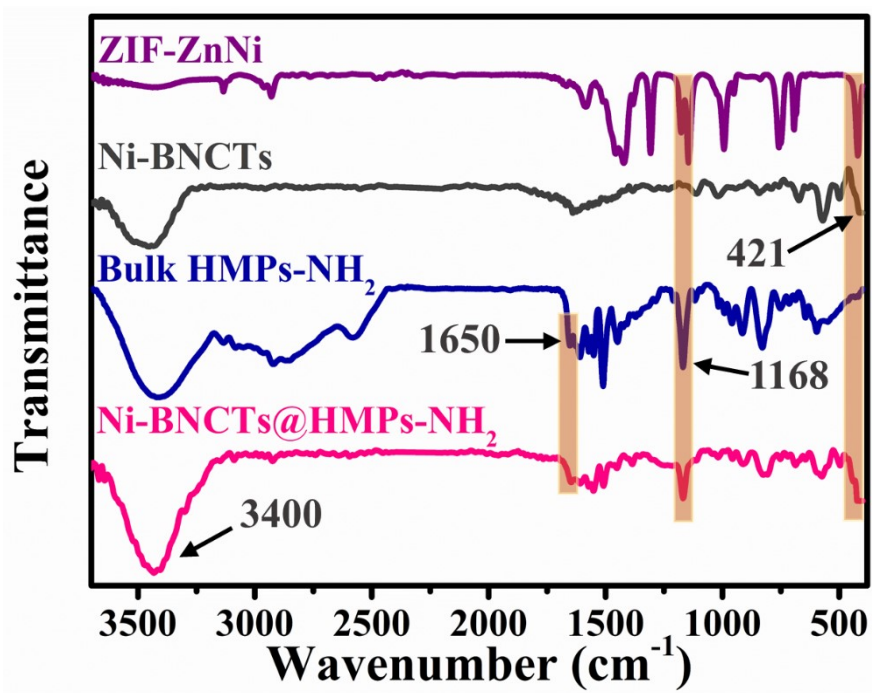
Figure S13. (a) FT-IR spectra of ZIF-ZnNi, Ni-BNCNTs, HMPs-NH$_2$, and Ni-BNCNTs@HMPs-NH$_2$.
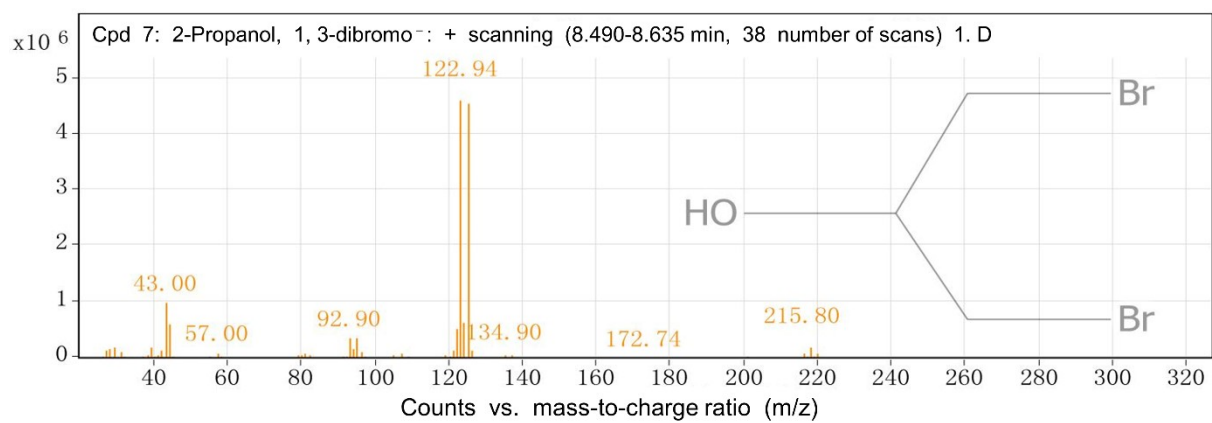
Figure S14. The GC-MS spectrum of generated ring-opened intermediate.
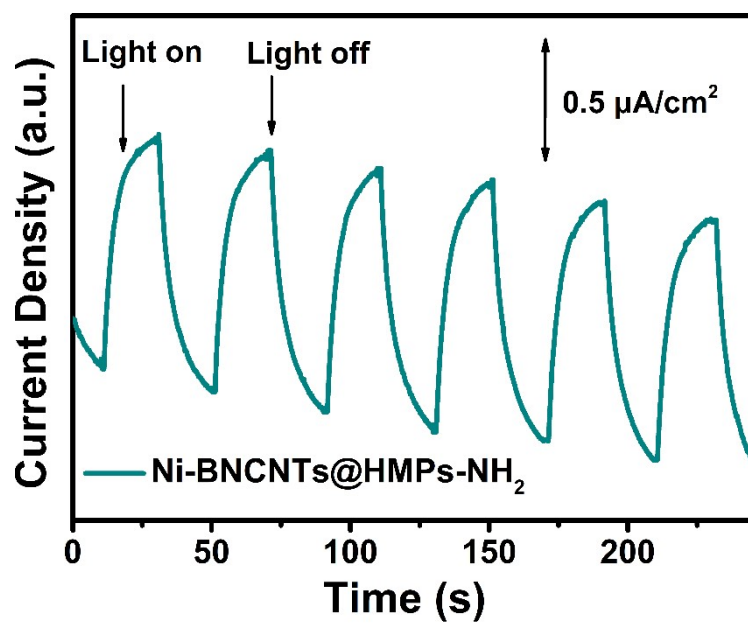
Figure S15. The photocurrent responses of Ni-BNCNTs@HMPs-NH$_2$.
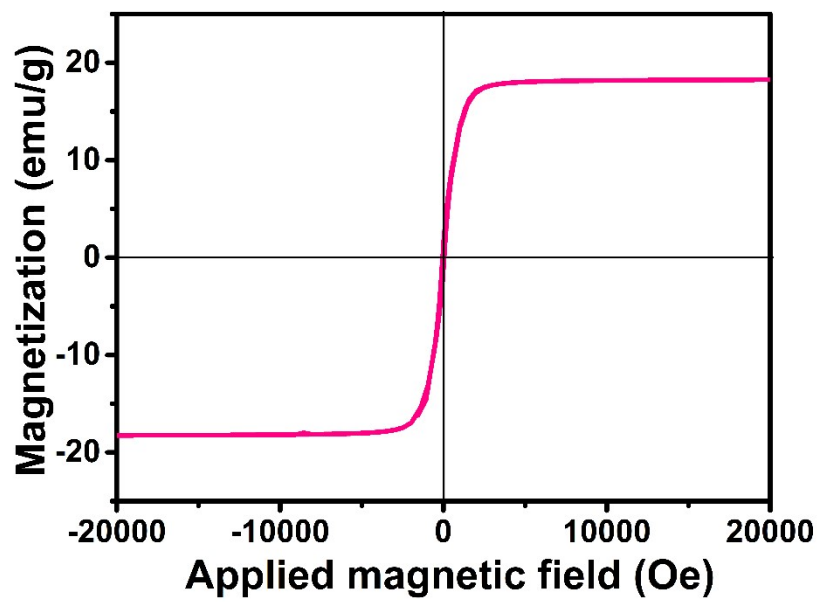
Figure S16. The magnetic hysteresis loop of Ni-BNCNTs@HMPs-NH$_2$.
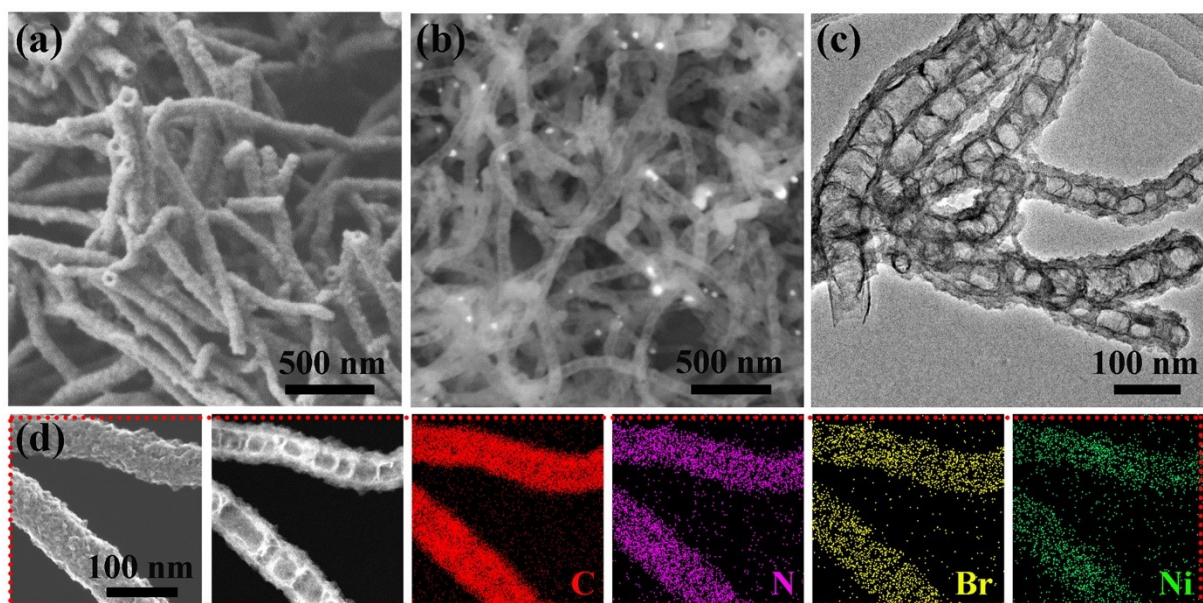
Figure S17. (a,b) SEM images and (c) TEM image of Ni-BNCNTs@HMPs-NH$_2$ after using for 10 times. (d) HAADF-STEM images and corresponding element mappings of Ni-BNCNTs@HMPs-NH$_2$ after using for 10 times.
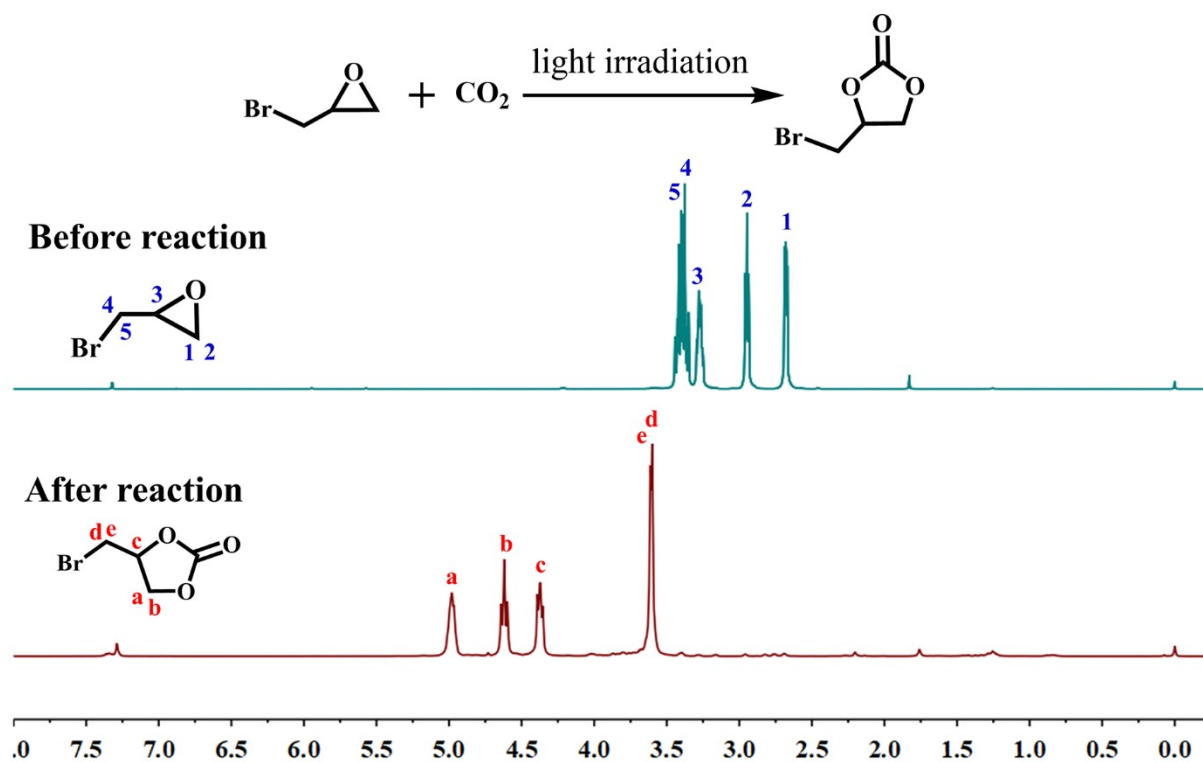
Figure S18. Crude ^{1}H-NMR spectra of cycloaddition of CO_2 with 2-(bromomethyl)oxirane by using Ni-BNCNTs@HMPs-NH$_2$ (Table 1, Entry 1).

4-(bromomethyl)-1,3-dioxolan-2-one. ^{1}H-NMR (400 MHz, CDCl$_3$): δ = 3.70-3.81 (m, 2H), 4.38-4.41 (dd, 1H, J = 4 Hz, J = 8 Hz), 4.56-4.60 (t, 1H, J = 8 Hz), 4.94-5.00 (m, 1H).

Figure S19. Crude ^{1}H-NMR spectra of cycloaddition of CO_2 with 2-(phenoxymethyl)oxirane by using Ni-BNCNTs@HMPs-NH$_2$ (Table 2, Entry 1).

4-(phenoxymethyl)-1,3-dioxolan-2-one. ^{1}H-NMR (CDCl$_3$, 400 MHz) δ 5.81-5.91 (m, 1H), 5.20-5.30 (m, 2H), 4.79-4.84 (m, 1H), 4.37-4.52 (m, 2H), 4.03-4.06 (m, 2H), 3.59-3.70 (m, 2H) ppm.
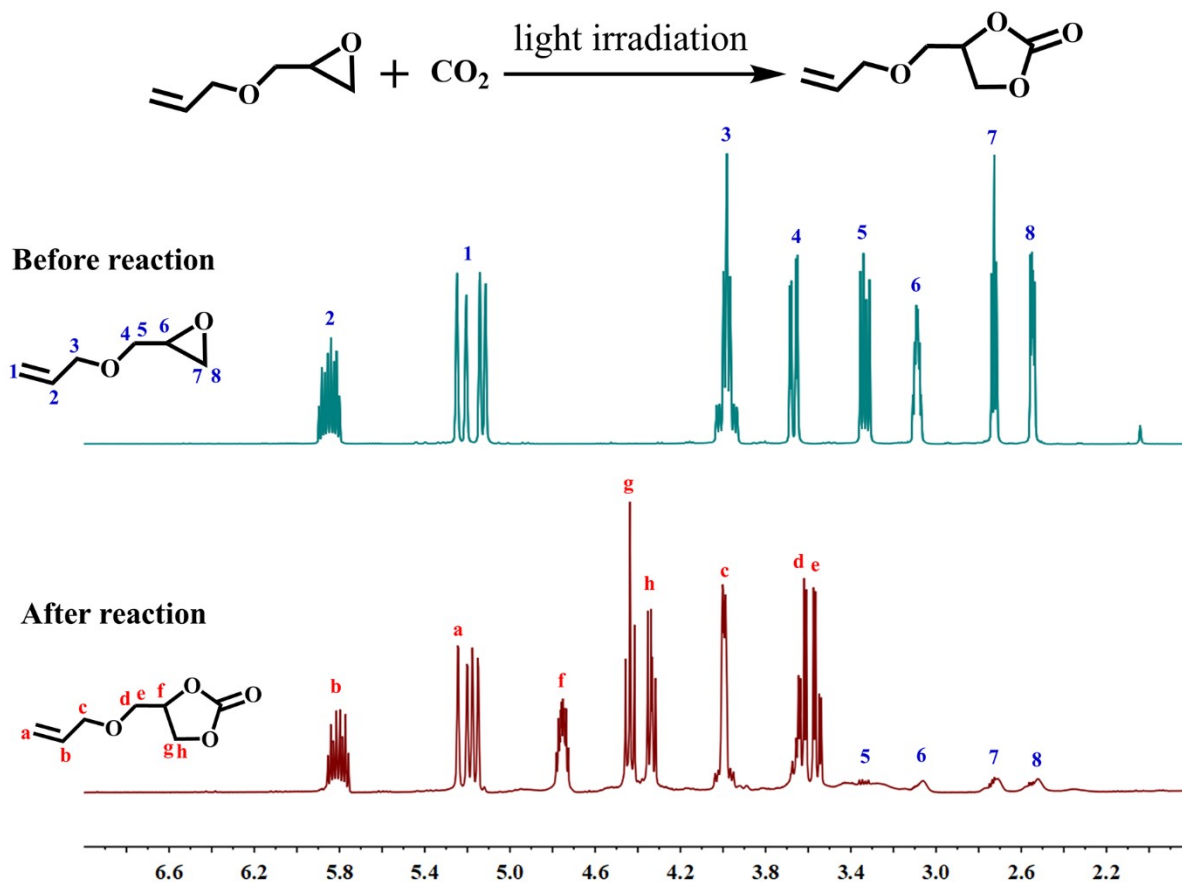
Figure S20. Crude ^{1}H-NMR spectra of cycloaddition of CO_2 with 2-((allyloxy)methyl)oxirane by using Ni-BNCNTs@HMPs-NH$_2$ (Table 2, Entry 2).

4-((Allyloxy)methyl)-1,3-dioxolan-2-one. ^{1}H-NMR (CDCl$_3$, 400 MHz) δ 5.81-5.91 (m, 1H), 5.20-5.30 (m, 2H), 4.79-4.84 (m, 1H), 4.37-4.52 (m, 2H), 4.03-4.06 (m, 2H), 3.59-3.70 (m, 2H) ppm.
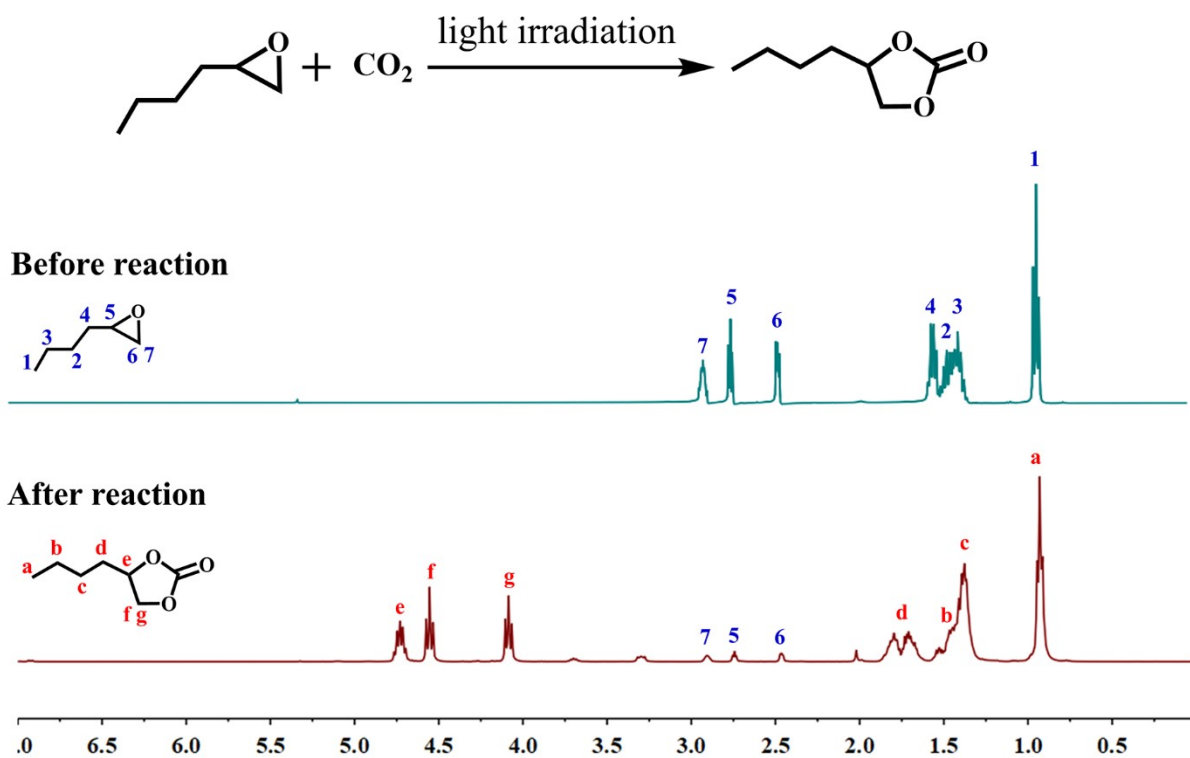
Figure S21. Crude ^{1}H-NMR spectra of cycloaddition of CO_2 with 2-butyloxirane by using Ni-BNCNTs@HMPs-NH$_2$ (Table 2, Entry 3).

4-n-Butyl-1,3-dioxolan-2-one. ^{1}H-NMR (CDCl$_3$, 400 MHz) δ 4.66-4.73 (m, 1H), 4.52 (t, J = 8.0 Hz, 1H), 4.06 (dd, J = 7.3 Hz, J = 8.0 Hz, 1H), 1.63-1.85 (m, 2H), 1.30-1.49 (m, 4H), 0.92 (t, J = 7.0 Hz, 3H) ppm.
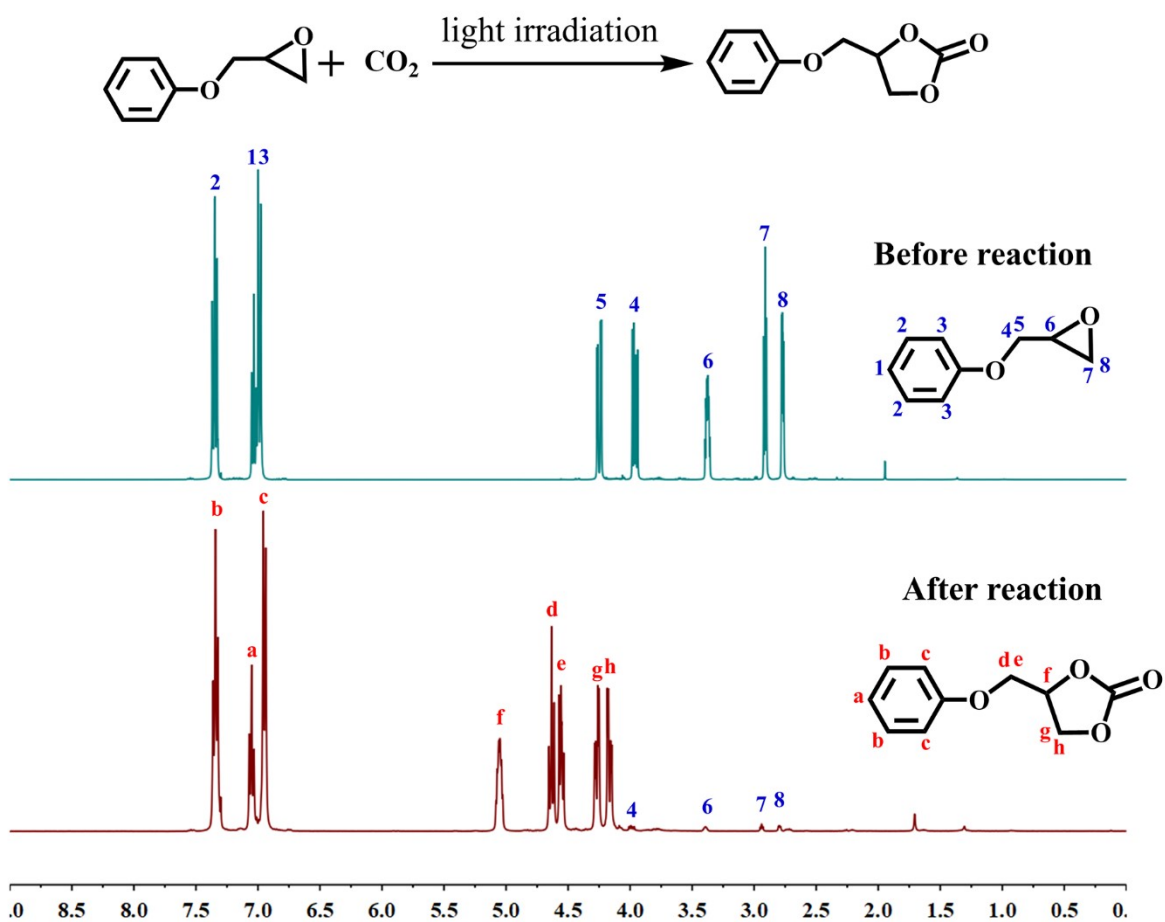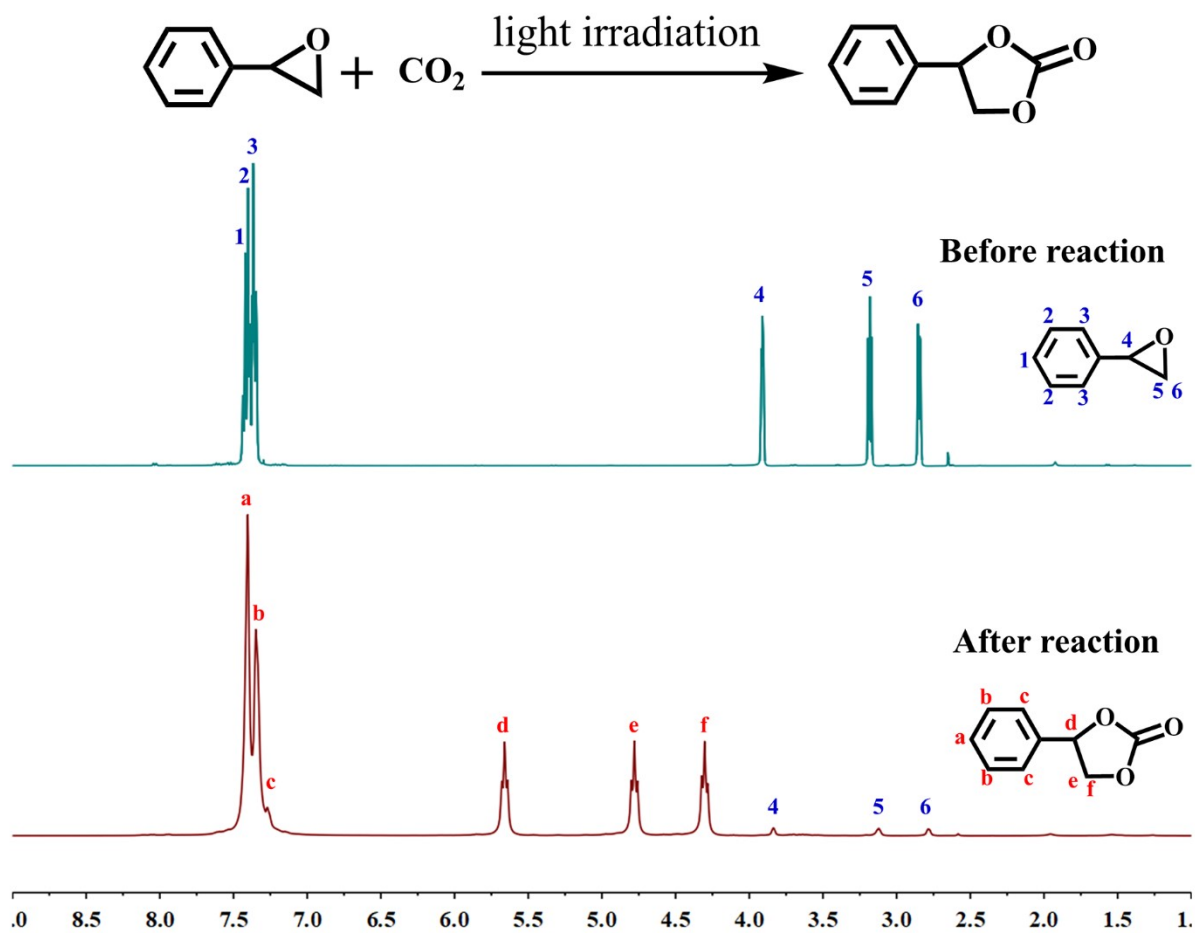
Figure S22. Crude ^{1}H-NMR spectra of cycloaddition of CO_2 with 2-phenyloxirane by using Ni-BNCNTs@HMPs-NH$_2$ (Table 2, Entry 4).

4-Phenyl-1,3-dioxolan-2-one. ^{1}H-NMR (CDCl$_3$, 400 MHz) δ 7.44 (d, 3J = 6.4 Hz, 3H), 7.36 (d, J = 7.6 Hz, 2H), 5.70 (t, J = 8.0 Hz, 1H), 4.80 (t, J = 8.4 Hz, 1H), 4.35 (t, J = 8.4 Hz, 1H) ppm.

Table S1. Structural parameters extracted from the Ni K-edge EXAFS fitting.

Sample	Scattering pair	CN	R(Å)	$\sigma^2(10^{-3}Å^2)$	$\Delta E_0(eV)$	R factor
Ni-BNCNTs	Ni-N	4.0	1.88	9.8	8.01	0.016

CN is the coordination number; R is interatomic distance (the bond length between central atoms and surrounding coordination atoms); σ^2 is Debye-Waller factor (a measure of thermal and static disorder in absorber-scatterer distances); ΔE_0 is edge-energy shift (the difference between the zero kinetic energy value of the sample and that of the theoretical model). R factor is used to value the goodness of the fitting.

Table S2. Summary of the previously reported catalysts and our catalyst for the cycloaddition of CO_2 with epoxides.

No.	Samples	Type	Epoxide	Co-catalyst/Solvent	CO_2 pressure (MPa)	T (°C)	Reaction time (h)	Yield (%)	Ref.
1	Co-POP	porous organic polymers	epichlorohydrin (8 mmol)	None/None	0.1	100	8	>99	1
2	COP-222	covalent organic polymer	epichlorohydrin (5 mmol)	None/None	0.1	100	24	99	2
3	rho-ZMOF	zeolite-like MOF	propylene oxide (34.5 mmol)	TBAB (0.62 mmol)/None	1	40	3	99.2	3
4	Amb-OH-I-910	Amberlite resin bead	propylene oxide (20 mmol)	None/Water	1	80	24	95	4
5	MOF-5-MIX	mesoporous nature	epichlorohydrin (25 mmol)	TBAB (0.25 mmol)/None	1.2	50	6	98	5
6	Phen$^+$-PHP-2Br	porous hybrid polymers	epichlorohydrin (2 mmol)	None/None	0.1	60	48	99	6
7	polyILs@MIL-101	MOF	3-bromopropylene oxide (1 mmol)	None/Acetonitrile	0.1	70	24	85	7
8	IHCP-OH(1)	microporous structure	epichlorohydrin (15 mmol)	None/None	3	135	1	99	8
9	Bi-PCN-224	MOF	propylene epoxide (4.5 mmol)	TBAB (0.5 mmol)/None	0.1	300 W xenon lamp	6	99	9
10	AuNPs-TBD	nanoparticles	propylene oxide (34.5 mmol)	TBAB (0.15 mmol)/None	0.1	780 nm LED	24	97	10
11	HPC-800	hollow structure	3-bromopropylene oxide (0.15 mmol)	TBAB (0.1 mmol)/DMF	0.1	0.3 W/cm^2	10	94	11
12	PMo$_{12}$@Zr-Fc	MOF nanosheets	styrene oxide (12.5 mmol)	TBAB (0.25 mmol)/None	0.1	0.4 W/cm^2	8	87	12
13	**Ni-BNCNTs@HMPs-NH$_2$**	**hierarchical porous**	**3-bromopropylene oxide (10 mmol)**	**None/None**	**0.1**	**0.4 W/cm^2**	**12**	**99**	**This work**

References

(1) Chakraborty, J.; Nath, I.; Song, S.; Kao, C.-M.; Verpoort, F. Synergistic Performance of a Sub-nanoscopic Cobalt and Imidazole Grafted Porous Organic Polymer for CO_2 Fixation to Cyclic Carbonates under Ambient Pressure without a Co-catalyst. *Journal of Materials Chemistry A* **2020,** *8* (28), 13916-13920, DOI: 10.1039/d0ta02821e.

(2) Subramanian, S.; Oppenheim, J.; Kim, D.; Nguyen, T. S.; Silo, W. M. H.; Kim, B.; Goddard, W. A.; Yavuz, C. T. Catalytic Non-redox Carbon Dioxide Fixation in Cyclic Carbonates. *Chem* **2019,** *5* (12), 3232-3242, DOI: 10.1016/j.chempr.2019.10.009.

(3) Zhang, S.; Jang, M.-S.; Lee, J.; Puthiaraj, P.; Ahn, W.-S. Zeolite-Like Metal Organic Framework (ZMOF) with a rho Topology for a CO_2 Cycloaddition to Epoxides. *ACS Sustainable Chemistry & Engineering* **2020,** *8* (18), 7078-7086, DOI: 10.1021/acssuschemeng.0c00885.

(4) Alassmy, Y. A.; Asgar Pour, Z.; Pescarmona, P. P. Efficient and Easily Reusable Metal-Free Heterogeneous Catalyst Beads for the Conversion of CO_2 into Cyclic Carbonates in the Presence of Water as Hydrogen-Bond Donor. *ACS Sustainable Chemistry & Engineering* **2020,** *8* (21), 7993-8003, DOI: 10.1021/acssuschemeng.0c02265.

(5) Kurisingal, J. F.; Rachuri, Y.; Gu, Y.; Choe, Y.; Park, D.-W. Multi-variate Metal Organic Framework as Efficient Catalyst for the Cycloaddition of CO_2 and Epoxides in a Gas-Liquid-Solid Reactor. *Chemical Engineering Journal* **2020,** *386*, 121700, DOI: 10.1016/j.cej.2019.05.061.

(6) Chen, G.; Zhang, Y.; Liu, K.; Liu, X.; Wu, L.; Zhong, H.; Dang, X.; Tong, M.; Long, Z. In Situ Construction of Phenanthroline-based Cationic Radical Porous Hybrid Polymers for Metal-free Heterogeneous Catalysis. *Journal of Materials Chemistry A* **2021,** *9* (12), 7556-7565, DOI: 10.1039/d0ta12018a.

(7) Ding, M.; Jiang, H.-L. Incorporation of Imidazolium-Based Poly(ionic liquid)s into a Metal-Organic Framework for CO_2 Capture and Conversion. *ACS Catalysis* **2018,** *8* (4), 3194-3201, DOI: 10.1021/acscatal.7b03404.

(8) Jia, D.; Ma, L.; Wang, Y.; Zhang, W.; Li, J.; Zhou, Y.; Wang, J. Efficient CO_2 Enrichment and Fixation by Engineering Micropores of Multifunctional Hypercrosslinked Ionic Polymers. *Chemical Engineering Journal* **2020,** *390*, 124652, DOI: 10.1016/j.cej.2020.124652.

(9) Zhai, G.; Liu, Y.; Lei, L.; Wang, J.; Wang, Z.; Zheng, Z.; Wang, P.; Cheng, H.; Dai, Y.; Huang, B. Light-Promoted CO_2 Conversion from Epoxides to Cyclic Carbonates at Ambient Conditions over a Bi-Based Metal-Organic Framework. *ACS Catalysis* **2021,** *11* (4), 1988-1994, DOI: 10.1021/acscatal.0c05145.

(10) Guselnikova, O.; Postnikov, P.; Kosina, J.; Kolska, Z.; Trelin, A.; Svorcik, V.; Lyutakov, O. A Breath of Fresh Air for Atmospheric CO_2 Utilisation: a Plasmon-assisted Preparation of Cyclic Carbonate at Ambient Conditions. *Journal of Materials Chemistry A* **2021,** *9* (13), 8462-8469, DOI: 10.1039/d0ta12530j.

(11) Yang, Q.; Yang, C. C.; Lin, C. H.; Jiang, H. L. Metal-Organic-Framework-Derived Hollow N-Doped Porous Carbon with Ultrahigh Concentrations of Single Zn Atoms for Efficient Carbon Dioxide Conversion. *Angewandte Chemie International Edition* **2019,** *58* (11), 3511-3515, DOI: 10.1002/anie.201813494.

(12) Fang, Z.; Deng, Z.; Wan, X.; Li, Z.; Ma, X.; Hussain, S.; Ye, Z.; Peng, X. Keggin-type Polyoxometalates Molecularly Loaded in Zr-ferrocene Metal Organic Framework Nanosheets for Solar-driven CO_2 Cycloaddition. *Applied Catalysis B: Environmental* **2021,** *296*, 120329, DOI: 10.1016/j.apcatb.2021.120329.